Title

Fatigue crack growth rates in high pressure hydrogen gas for multiple X100 pipeline welds accounting for crack location and residual stress

Authors

Ronevich, Joseph A
Song, Eun Ju
Feng, Zhili
et al.

Publication Date

2020-04-01

DOI

10.1016/j.engfracmech.2019.106846

Peer reviewed

Fatigue crack growth rates in high pressure hydrogen gas for multiple X100 pipeline welds accounting for crack location and residual stress

Joseph A. Ronevich[1], Eun Ju Song[1], Zhili Feng[2], Yanli Wang[2], Christopher D'Elia[3], Michael R. Hill[3]
[1] Sandia National Laboratories, Livermore, CA, USA
[2] Oak Ridge National Laboratory, Oak Ridge, TN, USA
[3] Department of Mechanical and Aerospace Engineering, University of California, Davis, Davis, CA, USA

Keywords: Hydrogen embrittlement, residual stress, welds, heat affected zone, fatigue crack growth rate

Submitted to *Engineering Fracture Mechanics*
Accepted and Published on-line Dec 2019, http://doi.org/10.1016/j.engfracmech.2019.106846

Abstract:

Fatigue crack growth rates (FCGR) of multiple X100 pipeline steel welds and heat affected zones were measured in high-pressure hydrogen gas to investigate their behavior compared to lower strength pipeline welds. A total of five high strength welds and two heat affected zones (HAZ) were examined all of which were fabricated using the same X100 base material. Different welding wires and techniques were used to fabricate the welds to provide a variety of end products to evaluate susceptibility to fatigue in high pressure hydrogen gas. Residual stresses were measured for each weld and HAZ using the slitting method and the effect of residual stress on the stress intensity factor, K_{res}, was determined. Using K_{res}, the fatigue crack growth rate curves were corrected to remove the effects of residual stress by examining the influence of K_{res} on stress ratio, R. Comparisons were then made between the high strength welds, which were corrected for residual stress, and lower strength welds from the literature. It was found that the higher strength welds and heat affected zones exhibited comparable fatigue crack growth rates to lower strength welds, as the FCGR data of the high strength welds overlaid the lower strength welds. This suggests that despite distinct differences in strength and microstructure between the different welds, hydrogen-assisted fatigue crack growth susceptibility is similar. A comparison was made between the K_{res} measured in extracted coupons and residual stress estimates provided in relevant welded pipe assessment standards such as API 579-1/ASME FFS-1. It was found the residual stress values in the test coupons extracted from welded pipe were significantly lower than those expected in the intact welded pipes and highlights the importance in quantifying and removing coupon residual stresses when fatigue crack growth rates are measured and including expected weld joint residual stress when making structural assessments.

1. Introduction:

Over 1,500 km of steel pipelines have been used to transport gaseous hydrogen throughout the U.S. safely and reliably over the years [1]. Hydrogen pipelines were constructed out of low strength steels and have been used to service refineries with relatively constant demand. The pipelines operate with minimal pressure fluctuations and modest pressures (<7 MPa). As a result, the safety history of these pipes has been relatively good over the years [1]. As an economy develops for alternative fuels, a greater demand is expected for hydrogen to help replace non-renewable energy resources, and steel pipelines can transmit gaseous hydrogen over long distances much cheaper than alternative methods such as by tanker

trucks [2]. One means to improve cost effectiveness of gaseous transmission of hydrogen is through operation at higher pressures to increase throughput. Lower strength steels which have conventionally been used in hydrogen pipelines may be limited in their operating pressures which prevents cost savings that could be realized by operating at higher pressures. Higher strength pipes offer a larger operating envelope for higher pressures and large diameter pipes to be used. As hydrogen demand fluctuates, there is potential for fatigue loading on pipelines which brings about a different failure mode that has not been examined on high strength steel pipeline welds. Recent work [3-9] has examined the behavior of a variety of strength grades of pipelines subjected to cyclic loading in hydrogen gas. The results showed similar accelerated fatigue crack growth for all the pipeline grades regardless of strength, which is counter to the conventional assumption that higher strength steels are more susceptible to hydrogen embrittlement. One area that has negligible research but needs to be investigated before higher strength pipes can be considered for deployment, is the behavior of welds in a cyclic hydrogen environment. Welds are a critical part of pipelines and often failures are associated with welds [10] yet the weld behavior under fatigue in the presence of hydrogen has not been explored, particularly in higher strength welds. The microstructure of welds is likely different than the base metals, although a comparison of FCGR for a variety of pipelines tested in high pressure hydrogen have shown negligible effects of microstructure [11]. Welds are more likely to have defects or stress concentrators due to misalignment or underfilling of the weld joint which could lead to initiation and extension of cracks. In addition, residual stresses are innate in welds which means that residual stress would be additive to the applied stress due to the gas pressure. Furthermore, higher strength welds are likely to retain higher residual stresses meaning the effects of residual stress could be more significant on the absolute stress experienced by the pipe. Only a few studies [4, 12, 13] have examined fatigue behavior of welds in hydrogen, which were from lower strength pipes, and residual stresses were not measured in these studies to examine their influence. One study [3] did examine a high strength weld and remove residual stress effects, but this was examined on a single weld and the results might not be applicable to other welding techniques and conditions. Residual stresses in welds and HAZs are complicated and depend on several factors such as materials to be welded, welding processes and parameters used, dimensions and geometry of the welded structure (such as plates vs pipes). Although the general characteristics of residual stresses maybe similar in trend, the specifics and magnitudes of the residual stress distribution could vary case by case. All of these factors motivate the current research to investigate the fatigue behavior of a broad range of high strength pipeline steel welds in high pressure hydrogen gas and examine the influence of residual stress on their behavior.

2. Methods

2.1 Weld fabrication

An experimental X100 girth welded pipe studied previously [3] was used as the test material for this study. The pipe is 19 mm thick with a diameter of 1.3 m and a measured yield strength of 731 MPa and ultimate tensile strength of 868 MPa in the longitudinal direction. The composition of the X100 pipe is listed in Table 1. As the X100 pipe was an experimental pipe (labeled as X100A), the details of the welding process were not provided including the filler wire used. From this original X100A welded pipe, sections of the base metal were removed in longitudinal strips such that subsequent welds were performed in the longitudinal direction, effectively making seam welds. From these X100A pipe sections, four welds were fabricated at Oak Ridge National Laboratory (ORNL) using different welding filler metals and different welding techniques. Tables 2a and 2b show a detailed list of the welding parameters. Three different filler metals were used for welds W1, W3, and W4 and a fourth weld was fabricated via friction stir welding

(FSW). W1 used matching strength filler metal ER100S-G from Lincoln Elec. W3 used over-matching filler metal ER120S-G from ESAB. The W4 weld used a novel welding consumable developed by ORNL in collaboration with the U.S. Army [14]. This weld consumable was specifically designed and formulated to prevent hydrogen embrittlement in welds of high-strength armored steels, based on the principle of low temperature phase transformation (LTPT) to reduce or eliminate the high tensile residual stresses in the weld region. In W4, a residual stress distribution was developed to promote compressive residual stress near the weld root. One of the advantages of using this weld wire is that it doesn't require pre-heat during fabrication of the weld, thus simplifying the welding process and reducing fabrication cost. For the FSW, pipe sections were welded longitudinally in a double-sided, double-pass, full penetration configuration. A Polycrystalline Cubic Boron Nitride (PCBN) tool was in the FSW. The tool had a threaded, tapered probe with three flats, 12 mm in length, and a convex, scrolled shoulder approximately 35 mm (1.4 inch) in diameter that engaged with the workpiece resulting in a weld crown width of approximately 25 mm (1 inch). The first pass of each stir weld was applied to the inner diameter (ID) of the pipe. The second pass was made from the outer surface side (OD) in the same welding direction as the first weld pass, overlapping the advancing side (AS) of pass 2 with the retreating side (RS) of pass 1 and the retreating side of pass 2 with the advancing side of pass 1.

Tensile testing was performed in air on samples perpendicular to the welding direction with the gage section encompassed both the weld and heat affected zones. Table 3 shows the resulting yield and tensile strengths of the five welds examined in this study. Failure often occurred in the HAZ as opposed to the weld metal, therefore only the YS and UTS values were reported. The nominal strain rate was 10^{-3}/s. Hardness maps of the welds are shown Fig. 1 for the X100 W1, W3, W4, and FSW showing the Vickers Hardness (VH) values. A hardness map was not collected of the X100A weld. All of the maps show a common trend; hardness values in the weld are equal to or greater than the base metal and reduced hardness in the HAZ, the HAZ softening effect commonly associated with welding of high strength steels. Two locations identified as (1) and (2) are shown in Fig. 1 for the FSW. These locations correspond to the micrographs of the FSW (Fig. 2g) and FSW-HAZ (Fig. 2h) and are discussed below.

Figure 2 shows scanning electron microscope images of the microstructures of the different welds and HAZ as compared to the original X100A base metal. The microstructure of the X100A base metal (Fig. 2a) consists of a mixture of fine ferrite and bainite. A variety of ferritic constituents are observed in the X100A weld and HAZ, W1, W3, FSW, and FSW HAZ but with varying densities. The HAZ microstructures exhibit lower strength constituents such as upper bainite and polygonal ferrite in the X100A HAZ (Fig. 2c) and X100 FSW HAZ (Fig. 2h), respectively. This change in microstructure was consistent with the lower hardness measured in the FSW HAZ as shown in Fig. 1. The X100 W4 represents the most unique microstructure, predominately martensite which is characteristic of the LTPT weld wire. Tempered martensite was also present in the inter-pass region, caused by the tempering effect of subsequent weld pass to the previous weld pass. It is important to note that the martensite of the LTPT weld wire in W4 weld is much more stable than the microstructure constituents in commercial weld wires in W1 and W3. It is particularly evident in the W3 weld, where the tempering effect from the subsequent weld passes substantially reduced the hardness (strength) of a weld pass from ~360Hv to the range of 250-300Hv. The microstructures of the high strength welds are much finer than observed in other lower strength welds in the literature [4, 12].

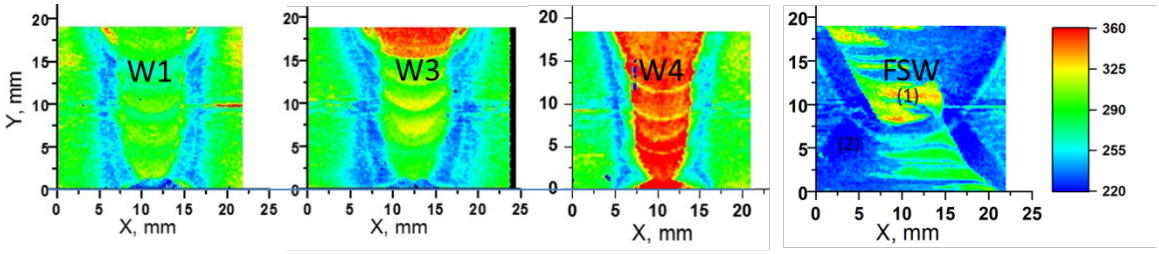

Figure 1 – Vickers hardness maps for the X100 W1, W3, W4 and FSW. No hardness data were collected of the X100A weld.

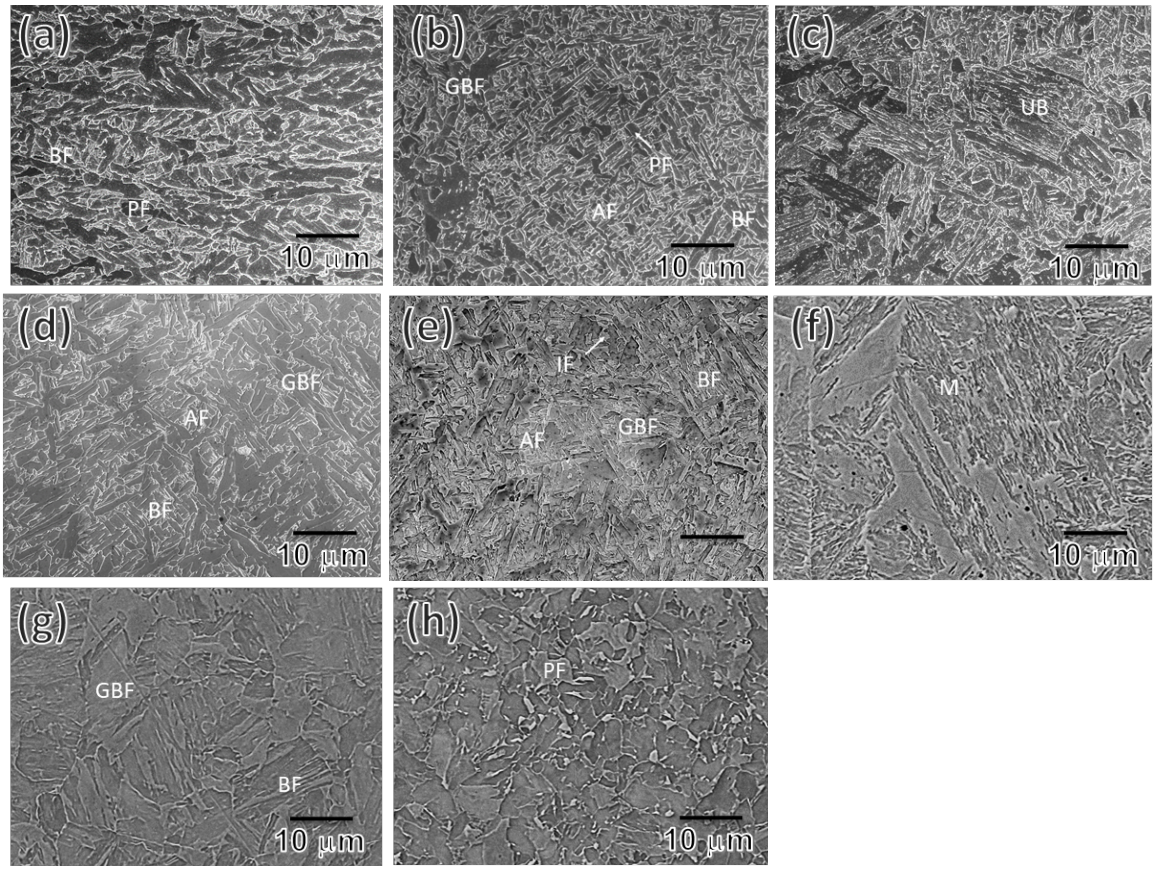

Figure 2 – Scanning electron microscope images of X100A base metal and X100 welds. (a) X100A base metal, (b) X100A weld, (c) X100A HAZ, (d) X100 W1, (e) X100 W3, (f) X100 W4, (g) X100 FSW, (h) X100 FSW HAZ. Different morphologies of ferrite and bainite are defined: GBF-grain boundary ferrite, AF-acicular ferrite, BF-bainitic ferrite, IF-idiomorphic ferrite, UB-upper bainite, M-martensite.

Table 1: Chemical Composition of X100A Base Metal (wt .pct)

Fe	C	Mn	P	S	B	Si	Cu	Ni	Cr	Mo	Nb	Ti	Al
Bal	0.085	1.69	0.013	<0.001	0.0015	0.26	0.14	0.24	0.19	0.17	0.047	0.017	0.029

Table 2a: Weld parameters of X100 W1, W3, W4

	W1	W3	W4
Root pass	ER70S-6 (pass 1)	ER70S-6 (pass 1)	LTPT HV 1764
Weld pass (2-6)	ER100S-G (Lincoln Elec.)	ER120S-G (ESAB)	LTPT HV 1764
Preheat	100C	125C	N/A
Inter pass Temp		125C	<55C
Shielding gas	Ar/Co2 (95/5), 1.13 CMH (40 CFH)	Ar/Co2 (95/5), 1.13 CMH (40 CFH)	Ar/Co2 (95/5), 1.13 CMH (40 CFH)
Heat input	Pass 1=370 kJ/m (9.4 kJ/in)	Pass 1= 413 kJ/m (10.5 kJ/in)	Pass 1=472 kJ/m (12 kJ/in)
	Pass 2-6 = 626-732 kJ/m (15.9-18.6 kJ/in)	Pass 2-6= 665-866 kJ/m (16.9-22 kJ/in)	Pass 2-5= 732-835 kJ/m (18.6-21.2 kJ/in)
Travel speed	Pass 1= 457 mm/min (18 in/min)	Pass 1= 457 mm/min (18 in/min)	Pass 1= 610 mm/min (24 in/min)
	Pass 2-6= 30.5 cm/min (12 in/min)	Pass 2-6= 25.4-30.5 cm/min (10-12 in/min)	Pass 2-6= 40.6 cm/min (16 in/min)

Table 2b: Weld parameters of X100 FSW

Parameter	Pass 1 & 2
Welding speed	50.8 mm/min
Tool Rotation Rates (welding)	125 rpm
Tool Rotation Rate (plunge)	270 rpm
Tool Tilt Angle	0 degrees
Axial Control Force Range*	75.62 kN

*Manually adjusted throughout each weld pass within this range

Table 3: Yield strength and ultimate tensile strength of fabricated welds

	X100A weld	X100 W1	X100 W3	X100 W4	X100 FSW
Yield strength (0.2% offset)	**705**	**580**	**720**	**740**	**605**
Ultimate tensile strength	**791**	**851**	**841**	**889**	**780**

2.2 Coupon Preparation

Test coupons were removed from the X100A welded pipe to allow for subsequent fatigue crack growth rate tests or residual stress measurements. Figure 3a shows a schematic of the orientations of coupon extractions for both the ESE(T) and C(T) coupons with respect to the original X100A pipe. As noted in Section 2.1, longitudinal sections of the X100A pipe were machined and seam welds were fabricated for the X100 W1, W3, W4, and FSW. For all ESE(T) coupons, the loading was applied perpendicular to the welding direction such that the crack extended in the through-thickness direction. The X100A weld was a girth weld, and loading was applied along the pipe longitudinal (L) direction with the crack growing in the radial (R) direction; this orientation is referred to as the L-R orientation. Welds X100 W1, W3, W4, and FSW were axial seam welds (as stated in Section 2.1 and shown in Fig. 3a) and loading was along the pipe circumferential (C) direction with the crack growing in the radial (R) direction; this orientation is termed C-R. ESE(T) coupons were machined with no side-grooves, a width

(W) = 12.7 mm, thickness (B) = 3.18 mm, and precrack starter notch length-to-width ratio (a_n/W) = 0.2. Figure 3b shows a schematic overlay of ESE(T) extraction location for a crack in the weld metal. Weld metal (weld) coupons had the notch positioned in the center of the weld with coupons for all welds tested: X100A weld and X100 W1, W3, W4, and FSW. In addition, coupons were extracted with a crack in the heat affected zone (HAZ) for two welds, with coupons designated as X100 FSW HAZ (Fig. 3c) and X100A HAZ (Fig. 3d). The X100 FSW HAZ coupon was removed in the C-R orientation and the X100A HAZ was removed in the L-R orientation. The notch of HAZ coupons were positioned outside of the weld metal (Fig. 3d) or stir zone (Fig. 3c) but still in the heat affected zones. The light grey regions (e.g. halo) shown in Figs. 3c and 3d are the etching response of the heat affected zones which is where the notches were positioned. A higher magnification image of the position of the notch is shown in Fig. 3d. The ESE(T) coupons were either used for FCGR measurements or residual stress measurements. Since both are effectively destructive tests, a minimum of two measurements of FCGR and residual stress were made on each weld to ensure consistency and allow for comparisons. In addition to the ESE(T) coupons with the machined notches, coupon blanks were removed from the FSW without the notch to facilitate easier measurement of residual stresses. In addition to the ESE(T) coupons, compact tension (C(T)) coupons were extracted from the X100A base metal and used for subsequent FCGR and residual stress measurements as reported in [3]. Because of material constraints in the thickness of the base metal, C(T) coupons were removed in the C-L orientation such that the loading direction was in the circumferential (C) direction and the crack propagated in the longitudinal (L) direction as shown in Fig. 3a.

2.3 Fatigue Crack Growth Measurements

Fatigue crack growth rate measurements were made on ESE(T) coupons in 21 MPa of high purity (99.9999%) hydrogen gas at room temperature, 293 K. Fatigue loading was accomplished using a servo-hydraulic load frame with a custom-built pressure vessel capable of delivering up to 22 kN of load dynamically to the sample. The system is built using dynamic spring energized Teflon® U-cup seals which allow for sealing between a pull-rod attached to the actuator and the pressure vessel. An internal load cell is located in the pressure vessel to ensure proper measurement of load on the coupon. Displacement was measured using a clip gauge. More details of the dynamic loading high-pressure system can be found in a previous publication [15]. Before beginning the test, air in the pressure vessel was removed via a process of evacuation and purging with high pressure helium. Four successive purges were performed with inert gas followed by vacuum for a minimum of 20 minutes, followed by four purges with hydrogen at 14 MPa, before filling the vessel to the test pressure of 21 MPa hydrogen. Oxygen contents were measured of the test gas following the completion of select tests and found to be consistently below 1 vppm. Duplicate and, in some cases, triplicate tests were performed on each weld at an applied load ratio of R_{app} = 0.5 and frequency of 1 Hz. The test pressure of 21 MPa was selected based on input from the ASME B31.12 Hydrogen Piping and Pipeline Code [16] committee and identified as an upper-bound for piping in the future. Test frequencies have been shown to only modestly affect FCGR [17]; e.g. FCGRs were observed to increase by a factor of 2 when test frequency was decreased from 1 Hz to 0.1 Hz and negligible changes were observed below that frequency for tests performed at constant ΔK of 17.5 MPa $m^{1/2}$. Fatigue crack growth rate tests were run according to ASTM E647-11 [18] as either constant load amplitude or positive K-control conditions. Results were consistent using either method. Crack length was determined using unloading compliance and a seven-point polynomial was used to develop da/dN vs. ΔK curves [18]. Following completion of the test, initial and final crack lengths were measured optically and used as fixed bounds to correct the crack lengths measured by unloading compliance.

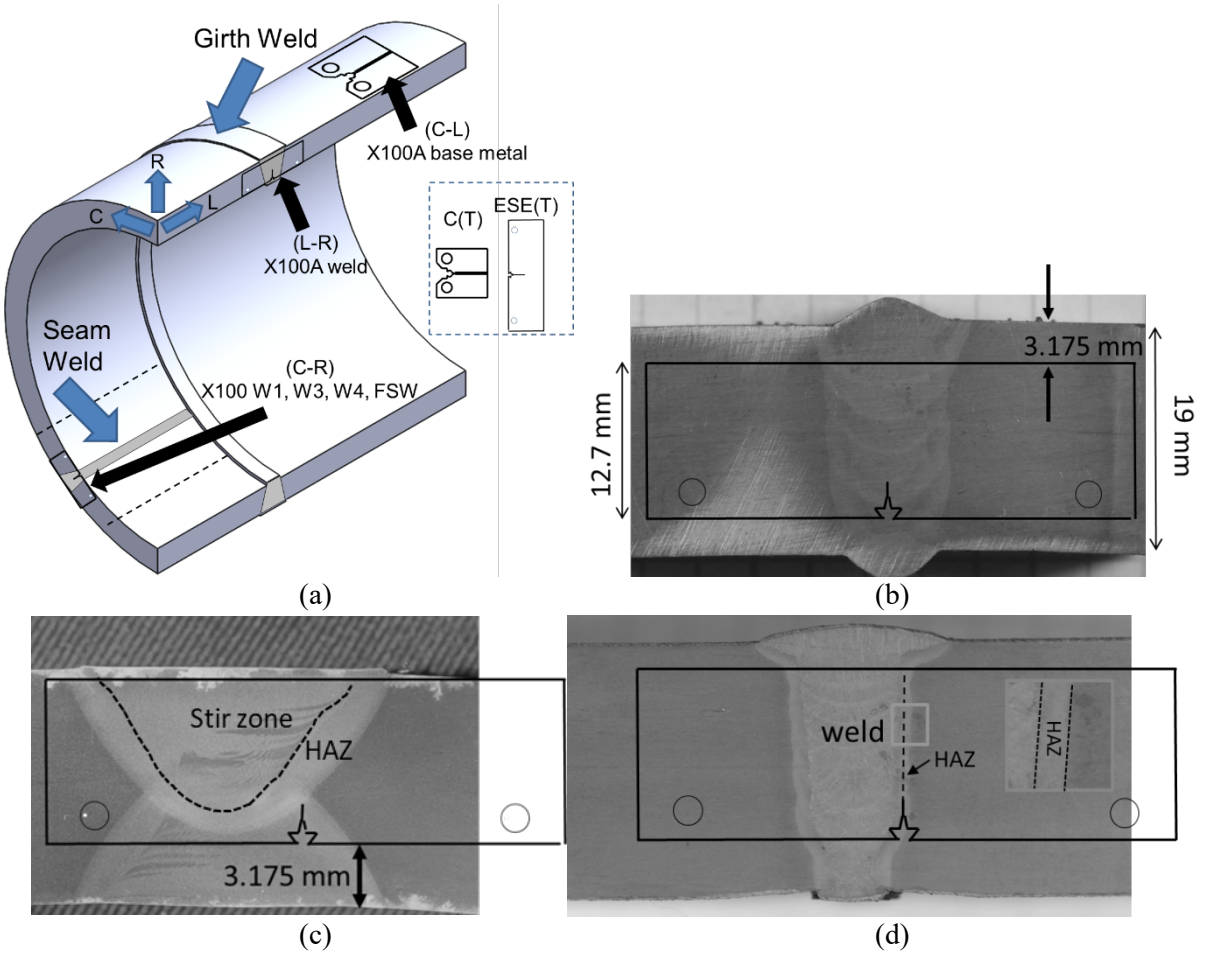

Figure 3 – (a) Schematic of extraction locations of C(T) and ESE(T) coupons from welded pipe. The dashed lines indicate that longitudinal sections of X100A base metal were removed and subsequent seam welds were fabricated. Schematic of ESE(T) coupon extraction locations from weld and HAZ for (b) X100 W1, (c) X100 FSW HAZ, (d) X100A HAZ. Notch was positioned in approximate center of weld or HAZ such that crack has stress in transverse direction with crack driving in the through-thickness direction from inner to outer diameter. All orientations are identified with respect to the original X100A welded pipe: L-Longitudinal, C-Circumferential, R-Radial.

2.4 Residual Stress Measurements

Residual stress along the crack plane of ESE(T) and C(T) coupons was measured using the slitting method [19-21]. Each coupon was fixed with a metallic foil strain gauge bonded to the coupon back face in line with the crack plane. A wire electric discharge machining (wire EDM) was used to extend a slit in increments of depth along the crack plane, from the notch or front face toward the back face. Residual stress as a function of distance from the front face, $\sigma_{res}(x)$ was determined from strain versus slit depth data, $\varepsilon(a)$, using typical procedures [20, 21]. The residual stress intensity factor as a function of crack length, $K_{res}(a)$ was also determined from strain versus slit depth data using the method described by Schindler [22]

$$K_{res}(a) = \frac{E'}{Z(a)} \frac{d\varepsilon(a)}{da} \tag{1}$$

where E' is the generalized planar elastic modulus, Z(a) is a geometry dependent influence function, and a is crack length. Plane stress was assumed and therefore the generalized elastic modulus was assumed to be E' = E = 207 GPa. The influence function Z(a) was available as an algebraic expression found in Schindler and Bertschinger [23]. The derivative dε(a)/da was determined by fitting a quadratic polynomial to a moving array of 5 strain data points and evaluating the polynomial derivative analytically [3]. The $K_{res}(a)$ and $\sigma_{res}(x)$ reported represent the stresses driving a crack in the radial through-wall direction of the welds in the ESE(T) coupons; however, because the C(T) coupons were extracted in the C-L orientation, the stress is the driving force for crack extension in the longitudinal direction.

2.5 Correction of Fatigue Crack Growth Rate Data Using Residual Stress Measurements

The following methodology for removing residual stress effects from FCGR curves measured on test coupons was outlined previously in detail in [3] and is briefly described below. All FCGR tests were conducted at an applied load ratio, $R_{app} = 0.5$ which is defined as the minimum load, P_{min}, divided by the maximum load, P_{max} as shown in equation 2

$$R_{app} = K_{min\text{-}app}/K_{max\text{-}app} = P_{min}/P_{max} \quad (2)$$

Residual stress (K_{res}) alters the total stress ratio, R_{tot}, by

$$R_{tot}(a) = (K_{min\text{-}app}(a) + K_{res}(a))/(K_{max\text{-}app}(a) + K_{res}(a)) \quad (3)$$

where $K_{min\text{-}app}(a)$ and $K_{max\text{-}app}(a)$ are the cyclic stress intensity factors at a minimum and maximum applied load. It is important to note that $R_{tot}(a)$ is dependent on the magnitude of $K_{res}(a)$; however, ΔK is independent of $K_{res}(a)$ as it appears in both the maximum and minimum stress intensity factors, effectively canceling (e.g. $\Delta K = \Delta K_{app}$). So any influence of $K_{res}(a)$ manifests itself as a change in total stress ratio (R_{tot}) not ΔK.

An analysis methodology was developed by Donald and Lados [24] and detailed by James [25] to collapse data of different stress ratios to a single curve which can be useful for design. The first step was to develop a normalized stress intensity factor (K_{norm}) that was independent of load ratio as shown below

$$K_{norm}(a) = (\Delta K(a))^{1-n} * (K_{max-app}(a) + K_{res}(a))^{n} \quad (4)$$

where n is a parameter for K_{max} sensitivity (n=1 makes K_{norm} depend only on K_{max} and n=0 makes K_{norm} depend only on ΔK). A value of $n = 0.25$ was determined by plotting three FCGR curves for X100A base metal tested in air at R =0.1, 0.5, and 0.7 and adjusting n to best visual fit when the plot of the three curves of da/dN vs K_{norm} collapsed [3]. The X100A base material was determined to be effectively residual stress free and did not exhibit crack closure [3]. As testing in this current study was only performed at $R_{app} = 0.5$, determination of n was not possible for each weld; however, the value of $n = 0.25$ is consistent with other structural metals reported in the literature [24, 25] and therefore was employed for all corrections in this current work on welds. Specific stress ratios $\bar{R}$ were then employed by using the K_{norm} curve and the Walker equation [25] as shown below

$$\Delta K_{corr} = K_{norm} * (1 - \bar{R})^{n} \quad (5)$$

where $n = 0.25$, $\bar{R}$ is 0.5, and the subscript corr indicates the data were corrected to account for the effect of varying $R_{tot}(a)$. In short, the data were corrected to force a stress ratio $\bar{R}$ equal to 0.5 even though the $R_{tot}(a)$ varied due to non-zero $K_{res}(a)$ in the welds.

3. Results and Discussion

3.1. Hydrogen accelerated fatigue crack growth measurements

The effect that hydrogen has on accelerating fatigue crack growth rates is easily observable in Fig. 4 which shows da/dN vs ΔK_{app} curves for high strength welds and heat affected zones tested in high pressure hydrogen gas. For comparison, fatigue crack growth rates were measured in air for X100A base metal and X100 W1 and W3 which exhibited significantly lower FCGR compared to in hydrogen, particularly in the higher ΔK range. Above ΔK = 10 MPa $m^{1/2}$, the effect of hydrogen on FCGR is apparent and FCGRs were measured to be more than an order of magnitude faster in hydrogen than in air. Five different X100 welds were examined in high pressure hydrogen gas and the heat affected zones (HAZ) were examined in two of the welds (X100A and X100 FSW). Duplicate (x2) or triplicate (x3) tests were performed on most welds and the results are plotted in Fig. 4. The exception is X100 W4 in which only 1 test was successful, which was attributed to large compressive residual stresses which made extending a precrack challenging. It should be noted that successful extension of a precrack of X100 W4 was only possible by compression precracking under load control from -0.89 kN to -5.340 kN to extend the precrack for approximately 30,000 cycles, followed by tension precracking to ~ a/W = 0.2.

In general, the results were repeatable for each weld tested. Observing the data as a whole, the characteristic trends are similar in that accelerated rates start between ΔK_{app} of 5 to 9 MPa $m^{1/2}$ and accelerate to over 30 times greater FCGR than in air at higher ΔK_{app} values. The band of FCGRs however appears to be quite broad when compared to FCGR trends observed for pipeline base metals tested in previous work [3-9] in which the curves nearly overlay regardless of the pipe grade. However, replicate tests exhibited self-consistency, which suggests real trends among the different welds examined which are discussed. First, in general, the HAZ exhibited lower FCGR than their respective welds for the X100A and X100 FSW. Second, the original X100A weld appears to exhibit the highest fatigue crack growth rate of all the welds tested. However, before any signicant conclusions can be made about these welds, it is important to note that although all the experiments were performed at applied load ratio of R_{app} = 0.5, the total stress ratio $R_{tot}(a)$ was actually quite different for each weld due to the influence of residual stress. It will be shown in the next section the influence that $K_{res}(a)$ has on $R_{tot}(a)$ and the shift that can occur in these FCGR curves when residual stress effects are removed.

Following the fatigue testing in high pressure hydrogen gas, the samples were fatigued in air to failure to allow observation of the fracture surfaces for further examination and measurement of crack extension. A representative set of fracture surface images is shown in Fig. 5 for the five welds tested, along with two HAZ and one weld tested in air. The distinct regions are identified in X100 W1 are the initial precrack, fatigue in H_2, and post fatigue in air. The gas metal arc welds exhibit distinct features on the fracture surfaces that have been attributed to the individual welding passes, as described in previous work [3]. These features are identified by the white arrows in Fig. 5 for the X100A weld and X100 W1, W3, and W4. The X100A HAZ, X100 FSW and X100 FSW HAZ do not exhibit these features, as metal was not added in layers in these regions as it was in the gas metal arc welds.

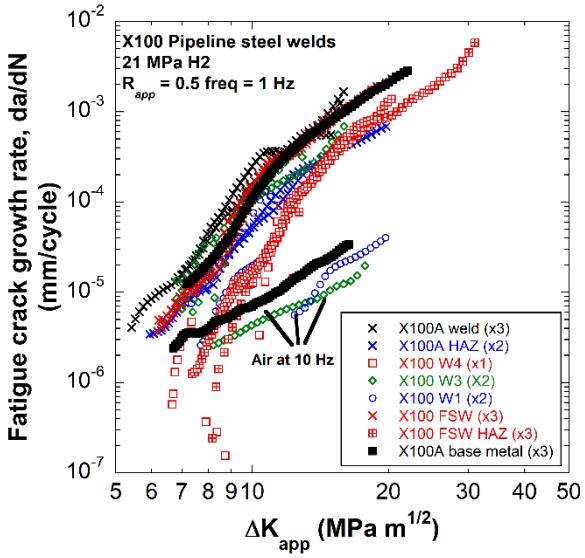

Figure 4 – Fatigue crack growth rate (da/dN vs ΔK_{app}) curves for X100 pipeline welds tested in 21 MPa H_2 gas at applied R=0.5 and frequency of 1 Hz. Tests were conducted in air at 10 Hz for comparison.

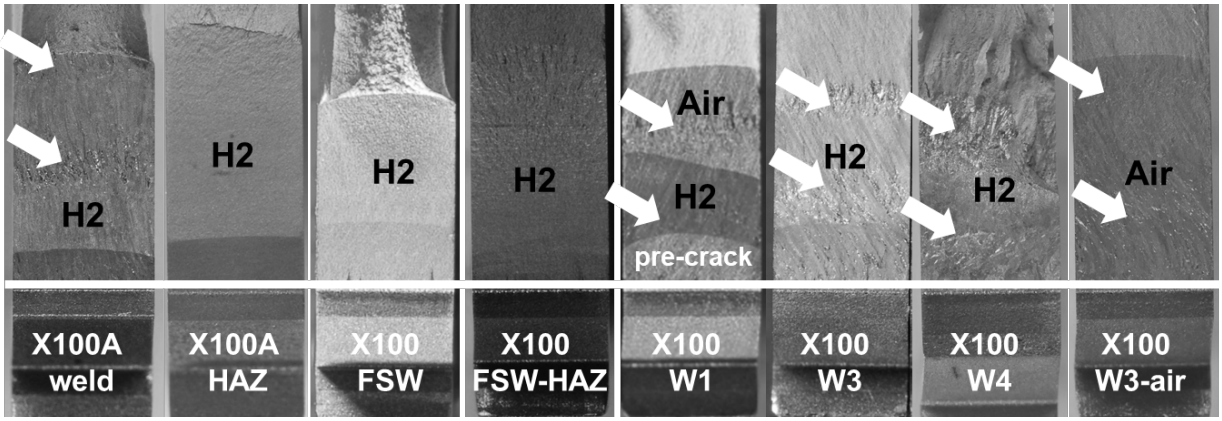

Figure 5 – Fracture surfaces of X100 welds tested in 21 MPa H_2 gas and in air. Three distinct regions are visible on most fracture surfaces as the crack extends from bottom to top as labeled in X100 W1: pre-crack in air, fatigue in H2, and post fatigue in air. Multi-pass arc welds (e.g. X100A weld, W1, W3, W4) are distinguishable by periodic rough features associated with individual weld passes (white arrows).

3.2. Residual stress measurements in test coupons

Using the slitting method, residual stress as a function of distance from the front face was measured for the 5 weld, 2 HAZ, and X100A base metal coupons, with data shown in Fig. 6. Duplicate tests were performed and show excellent repeatability which are plotted in Fig. 6 except for on X100 W4 in which only a single test was performed. The duplicate tests overlay each other demonstrating the consistent residual stresses in the test coupons. In most weld coupons, the measurements started from the existing machined notch, beginning around 2.5 mm from the front and extended to approximately 12 mm. The X100 FSW and X100 FSW HAZ samples were prepared without a notch so those measurements began

approximately 0.5 mm from the front face. In all weld and HAZ coupons, x = 0 mm was closest to the inner diameter of the pipe with x increasing radially outward, as shown in Fig. 3a. A C(T) coupon was used for measurements on the X100A base metal which has a larger notch, and therefore, measurements were not obtained until approximately 5 mm from the load line. All of the weld and HAZ coupons exhibited significant residual stress levels which varied predominantly between +/- 200 MPa with some deviations outside of this range. Most notable is the X100 W4 which contained a highly compressive stress over -500 MPa around 3 mm. Repeated fluctuations in the residual stress with distance were attributed to the periodic weld passes and are more prevalent in the gas metal arc weld samples than the FSW or HAZ samples.

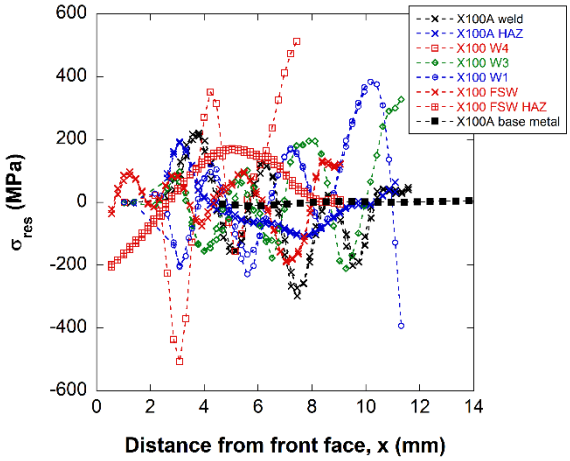

Figure 6 – Residual stress (σ_{res}) as a function of distance (x) from front face for X100 welds and base metal. For each weld, two separate samples were measured, and the results are plotted, except for X100 W4 which is only a single test. Negligible residual stress was measured in X100A base metal.

The residual stress intensity factor, K_{res}, as a function of crack length data from all coupons are shown in Fig. 7. Duplicate tests show good repeatability and there are significant differences in K_{res} for the different weld and HAZ coupons. In Fig. 7, the periodicity in K_{res} is more prevalent for the multi-pass weld coupons compared to the smooth trends for the FSW and HAZ coupons. The X100 FSW HAZ coupons exhibited a negative K_{res} at short crack lengths decaying to negligible values at longer crack lengths. The X100 W4 coupon exhibited large negative K_{res} values at short crack lengths which diminished at longer crack lengths. The X100A weld and HAZ coupons exhibited positive K_{res} at short crack lengths that diminished to negligible values at longer crack lengths. Positive and negative K_{res} values were measured in the X100 FSW, W1, and W3 coupons depending on crack position. The K_{res} values shown in Fig. 7 are a weighted integral of residual stress (Fig. 6); therefore the slope of K_{res} versus a is positive when the σ_{res} is positive and vice versa.

Total stress ratio $R_{tot}(a)$, calculated using Eq. 3, is shown in Fig. 8a for all coupons. Note that the R_{app} was equal to 0.5, therefore any deviation of $R_{tot}(a)$ from 0.5 is direct influence of $K_{res}(a)$, which is quite substantial in some coupons. At longer crack lengths the $R_{tot}(a)$ values approached 0.5 but at shorter crack lengths a significant amount of variability was observed except for the X100A base metal which exhibited $R_{tot}(a) \sim R_{app} = 0.5$. The X100A weld, X100A HAZ, and X100 FSW all exhibited $R_{tot}(a)$ values greater than 0.5 for the majority of the fatigue test. X100 W1, X100 W3, X100 W4 and X100 FSW HAZ all exhibited $R_{tot}(a)$ values less than 0.5. Of notable interest is the X100 W4 at short crack lengths which actually exhibited negative $R_{tot}(a)$ suggesting compression loading during portions of the fatigue test. This is due to the extremely large negative K_{res} at short crack lengths. This also perhaps explains the unconventional behavior of the da/dN vs ΔK_{app} curve for the X100 W4 shown in Fig. 4 which exhibited very low fatigue

crack growth rates and discontinuities in the curve. Testing at negative R would have the effect of lowering the FCGR substantially. Due to the presence of the notch and precrack in ESE(T) coupons, the majority of the FCGR data were collected between 4 and 9 mm crack lengths. Therefore, because $R_{tot}(a)$ is calculated based on K_{max} and K_{min} data from FCGR curves, only the $R_{tot}(a)$ values experienced in the tests are shown (e.g. no $R_{tot}(a)$ values were calculated from crack lengths less than 4 mm or longer than 9 mm except for the X100A base metal which was performed on a C(T) coupon). In Fig. 8b, the $R_{tot}(a)$ values were also plotted versus ΔK_{app}. It should be noted that $R_{tot}(a)$ does not depend solely on ΔK_{app} but rather $K_{res}(a)$ measured from the slitting experiments, as well as $K_{max\text{-}app}$ and $K_{min\text{-}app}$ as shown in Eq. 3. However, because the FCGR tests were performed as increasing ΔK_{app} tests, the comparison in Fig. 8b allows for easier interpretation of the effect of $R_{tot}(a)$ on the FCGR curves plotted in Fig. 4. As Fig. 8b shows, the $R_{tot}(a)$ was the most variable at lower ΔK_{app} and trended towards 0.5 at higher ΔK_{app}.

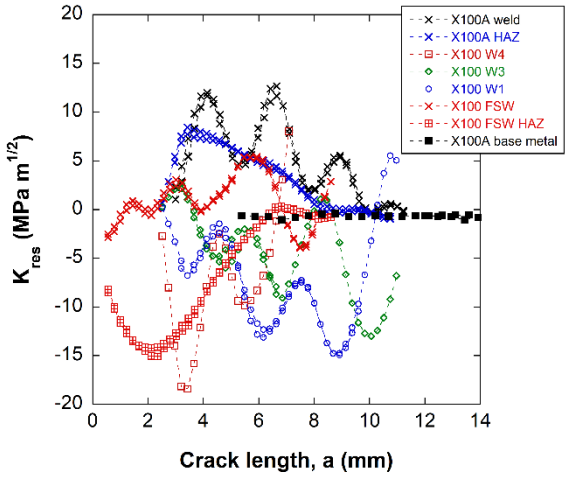

Figure 7 – Residual stress intensity factor (K_{res}) as a function of crack length for X100 welds and base metal. For each weld, two separate samples were measured, and the results are plotted, except for X100 W4. The periodicity observed in the gas metal arc welds is consistent with the individual passes present in these multi-pass welds.

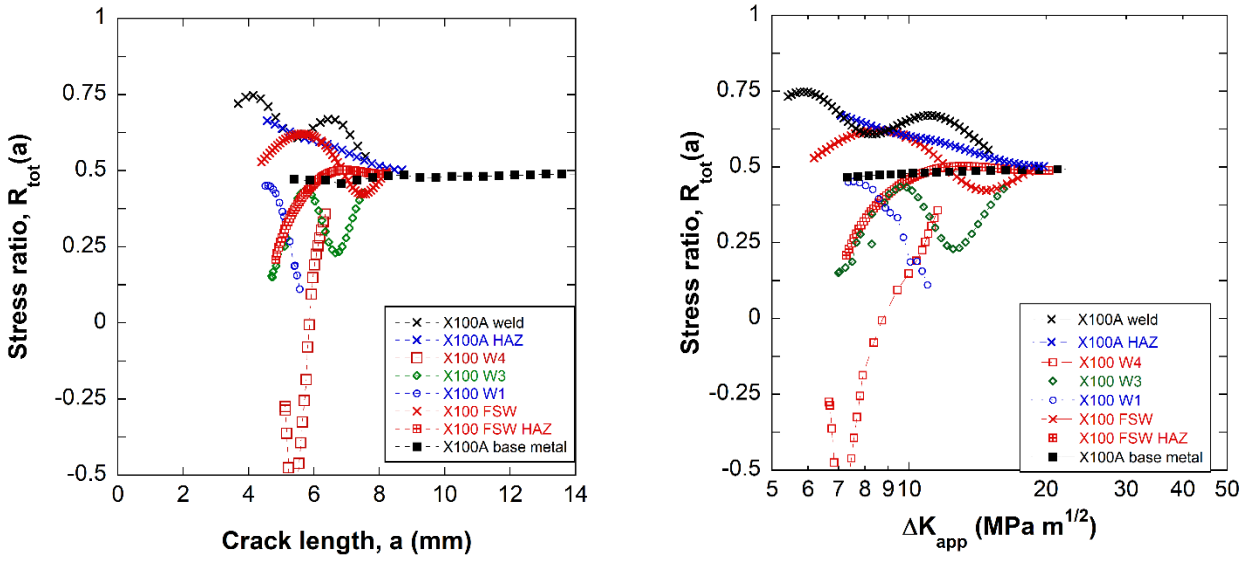

(a) (b)

Figure 8 - (a) Total stress ratio, $R_{tot}(a)$, as function of crack length for the X100 welds, base metal and HAZ. (b) Total stress ratio, $R_{tot}(a)$, as a function of ΔK_{app} to show that the largest deviations from the $R_{app} = 0.5$ were at the lower ΔK_{app}. $R_{tot}(a)$ values were negative for X100 W4 for the majority of the lower ΔK_{app}.

3.3 FCGR correction using K_{res}

Fatigue crack growth rate curves were corrected (da/dN vs. ΔK_{corr}) by removing the effects of residual stress. This was accomplished by collapsing the data to a single K_{norm} curve according to Eq. 4 and then re-introducing the specified stress ratio $\bar{R} = 0.5$ as described in section 2.5. The resulting FCGR curves are shown in Fig. 9 for the X100 welds, HAZs, and base metal. The term ΔK_{corr} is used to indicate that the data have been corrected for residual stress. In addition, three curves in air for the X100A base metal, X100 W1, and X100 W3 are shown for comparison. Similar to Fig. 4, duplicate (x2) or triplicate (x3) test results are shown except for X100 W4 (x1) in which only a single test was performed.

In general, the FCGR curves exhibit greater overlap and occupy a tighter band when corrected for residual stress as shown in Fig. 9 compared to the da/dN vs ΔK_{app} data in Fig. 4. As would be expected, the materials with the largest K_{res} exhibited the greatest shift in FCGR curves (e.g. X100 FSW HAZ and X100 W4). Because both had compressive residual stresses (e.g. negative K_{res}), their $R_{tot}(a)$ values were less than 0.5 and when plotted at the specified stress ratio $\bar{R} = 0.5$, the curves shifted to the left in ΔK-space when corrected. It is commonly observed that testing at higher R shifts the curve to the left and vice versa [26]. A comparison of the FCGRs in air also shows the data overlay better after corrected for residual stress (Fig. 9) than in the raw data (Fig. 4). The X100A base metal contained negligible residual stress and as a result did not shift when corrected for residual stress; therefore, X100A base metal can serve as a reference curve between the two figures (Fig. 4 and Fig. 9). It is interesting to note that the majority of FCGR curves in 21 MPa H_2 fall below the X100A base metal data which suggests that in the absence of residual stress, the welds and HAZs microstructures are not more susceptible to accelerated fatigue crack growth rate than the base metal. While accounting for residual stress reduces variability in FCGR, variability remains in Fig. 9. This may be partially due to limitations of the residual stress correction scheme adopted here but may just as likely be attributed to other sources of location-to-location and part-to-part variations in welded materials.

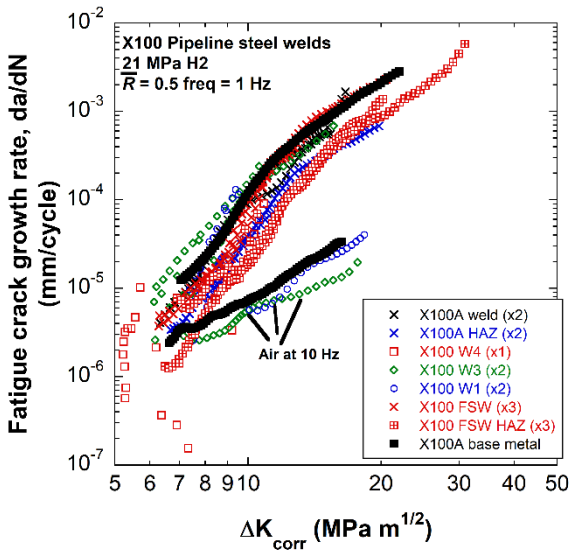

Figure 9 – Fatigue crack growth rate curves (da/dN vs ΔK_{corr}) corrected for residual stress for X100 welds, base metal and HAZ tested in 21 MPa H_2 at specified stress ratio $\bar{R}$ = 0.5 and 1 Hz.

3.4 Comparison of High Strength Welds with Low Strength Welds

One motivation for investigating the fatigue behavior of higher strength welds in hydrogen was to determine their general susceptibility relative to lower strength grades more commonly used. In the literature [4, 12, 13], several lower strength pipeline welds have been tested in similar hydrogen environments; however, residual stress measurements have not been performed on the lower strength welds. Therefore, a true comparison of the residual stress-free FCGRs cannot be conducted. However, given that lower strength welds have a lower capacity for residual stress, it was thought that comparisons could be made between residual stress-free X100 weld FCGR curves and the non-corrected lower strength welds. It should be noted that the FCGR data on lower strength welds found in refs [4, 12] were generated in the same laboratory as the current work and therefore should provide some consistency in procedures to allow for comparisons. To simplify the comparison, Fig. 10 shows the upper and lower bound data for the X100 welds and HAZ (extracted from Fig. 9) compared to lower strength welds from the literature [4, 12, 13]. In addition, the X100A weld was plotted in Fig. 10 along with the master design curve for pipeline steels found in the newly approved version of ASME B31.12 code. Currently, the B31.12 master curve can only be used for pipelines with specified minimum yield stress (SMYS) up to 482 MPa (70 ksi) operating up to 21 MPa H_2. The lower strength welds [4, 12, 13] were tested at nominally the same conditions as the current study; however, residual stress measurements were not performed and therefore the plots are in the form of da/dN vs ΔK_{app}, indicated by the (*). The X100A weld and the upper and lower bound curves are plotted with respect to ΔK_{corr} which were corrected for residual stress. The lower strength welds exhibit very similar FCGRs and clearly fall within the upper and lower bounds as shown in Fig. 10. In addition to being lower strength, the microstructures of the X52, X65, and X70A welds are unique compared to the X100 welds, yet the FCGR behavior fall within the bounds of the high strength welds. Furthermore, the ASME B31.12 design curve for pipelines falls close to the upper bound high strength weld data signifying that the B31.12 master curve may suffice in capturing the majority of higher strength weld data. This suggests that higher strength welds without residual stress do not exhibit significantly greater susceptibility to accelerated FCGR than lower grades containing residual stress. It also demonstrates that microstructural differences do not

appear to have a significant effect on the susceptibility to hydrogen-accelerated fatigue crack growth and that the dominate effect in shifting FCGR curves is residual stress.

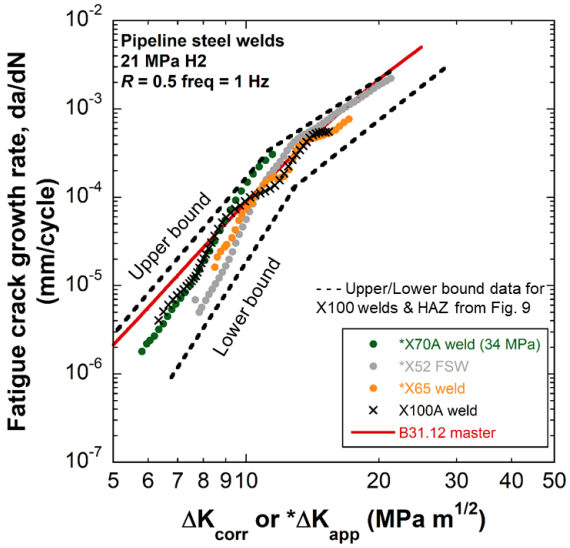

Figure 10 – Fatigue crack growth rate curves for lower strength welds compared to upper and lower bound data of residual stress-free FCGR curves for high strength welds and HAZ (extracted from Fig. 9). Curves for high strength welds (e.g. X100 welds) were corrected for residual stress and are therefore plotted versus ΔK_{corr}. Lower strength welds are not corrected for residual stress and are plotted versus ΔK_{app}. Welds of X52 [4], X65 [12] and X70 [13] were all performed at R_{app} = 0.5. X100A weld and ASME B31.12 master design curves are shown for comparison.

3.5 Importance of Residual Stress Impacts on FCGR

It was shown in the previous sections that residual stresses and K_{res} affect the total stress ratio, $R_{tot}(a)$, which shifts FCGR data found in coupon tests, e.g. higher R_{tot} shifts the FCGR higher and vice versa. The literature [26, 27] also shows that K_{max} influences the onset of hydrogen accelerated fatigue crack growth (HA-FCG) and K_{max} is also affected by K_{res}.

It is important to underscore that residual stress impacts fatigue engineering in two distinct ways. First, residual stress effects occur in FCGR tests and it is useful to remove those effects so that FCGR data are useful in design, for alloy-to-alloy comparisons, and to enable comparisons of intrinsic FCGR resistance in different regions of welded joints (e.g., base metal, weld, and HAZ). Second, welded connections in structures have residual stresses that are distinct from those in coupons, and these residual stress fields are often larger. Accounting for these two distinct contributions of residual stress is important, and particularly for welds in higher strength materials because of their capacity to retain higher residual stresses.

In the current study, residual stress and K_{res} were measured on rectangular ESE(T) coupons extracted from approximately the mid-thickness of 19 mm thick pipe (Fig. 3). The levels of residual stress are modest, with peak values of 20 to 40% of the base metal yield strength. The levels of K_{res} are also modest, being less than 20 MPa $m^{1/2}$, because the residual stresses are small and because the stresses have no net uniform or bending component (which must be the case in a free-standing coupon); in all cases the values of K_{res} decrease to negligible levels at long crack lengths. Residual stresses relax as a result of coupon

removal, so the coupon residual stresses are most certainly different than those in the intact welded pipe. The difference between coupon and intact residual stress fields further reinforces the importance of removing the effect of residual stresses from the FCGR data as the residual stress effects are not representative of those in intact pipe welds.

Residual stresses in intact piping should be included in structural assessments and it is instructive to compare typical intact piping residual stress fields and corresponding K_{res} values to the data from the present coupons. Relevant welded piping assessment standards [28, 29] provide guidance on the magnitude and distribution of residual stress typical of piping weld joints. The guidance includes residual stress magnitude and spatial distribution depending on factors such as material strength, weld type, joint thickness, and heat input [28, 29]. Annex 9D.5 of API 579-1/ASME FFS-1 [29] provides equations for estimated residual stress perpendicular to the weld, based on strength and heat input. Heat input ($\dot{q}$) normalized by pipe thickness is categorized as high (> 120 J/mm^2), medium (> 50 J/mm^2), or low (< 50 J/mm^2). All of welds in this study, which we have data for, have low heat input ranging from 33 to 46 J/mm^2. Fig. 11 shows these residual stress distributions, assuming σ_{YS} = 731 MPa for X100A base metal and a pipe thickness of 19 mm. When compared to the residual stresses measured in the removed ESE(T) coupons (Fig. 6), all of the simulated residual stresses for intact pipes in Fig. 11 have large magnitude. They also include significant uniform (low and medium heat input) and bending (high heat input) fields that are absent in the coupon residual stresses (they must be absent in a free-standing coupon, on account of equilibrium constraints). Figure 11 also shows that the low heat input weld has the most conservative recommended residual stress distribution (e.g. largest average tensile residual stresses throughout the thickness).

Given the large differences in residual stress, values of K_{res} in a cracked pipe would also differ greatly from the values of K_{res} found in the FCGR coupons. Using the low heat input residual stress field in Fig. 11 we computed K_{res} using the weight function method from ASME Section XI Appendix A [30] assuming a circumferential flaw driven by the axial residual stress. The flaw shape was assumed semi-elliptical with an aspect ratio of 1/3 (depth divided by total surface length), which is conservative according to ASME BPVC Section VIII Div 3 Article KD-4 [31]. Fig. 12 compares K_{res} for the pipe weld to K_{res} measured in the removed FCGR coupons. This shows clearly that K_{res} in the FCGR coupons differs substantially from what should be expected in a pipe weld, being far lower in the coupons, and suggest the significant release of residual stress occurring upon coupon extraction.

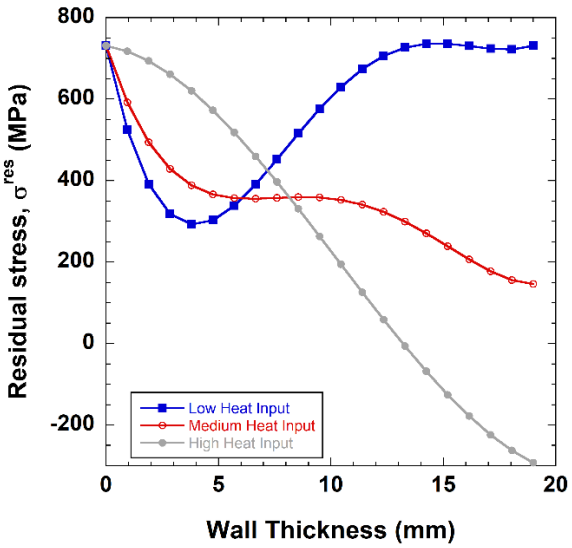

Figure 11 – Recommended residual stress (σ^{res}) distributions perpendicular to the weld for low, medium, and high heat input welds as a function of position through-wall. Plot was developed using YS=731 MPa, and t = 19 mm.

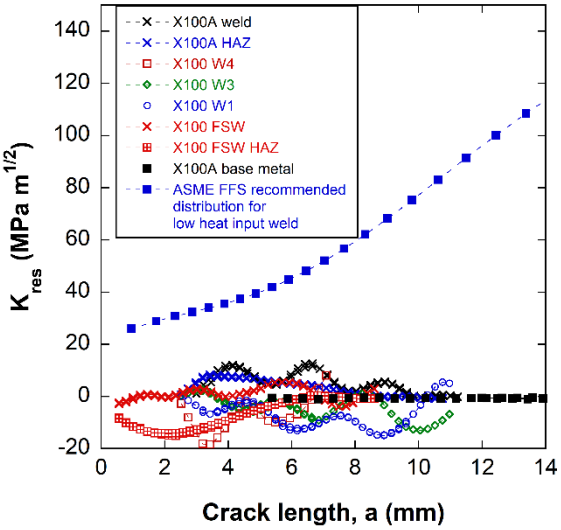

Figure 12 – K_{res} vs crack length for X100 welds, HAZ, and base metal compared to K_{res} recommended distribution for full thickness low heat input weld according to API 579/ASME FFS-1 [29]. The recommended K_{res} plotted is for a flaw in the radial direction with stress applied in the longitudinal direction. This orientation is consistent with the measured K_{res} for the X100A weld and X100A HAZ. The K_{res} for the seam welds are also for a flaw in the radial direction, however the stress applied is in the circumferential direction. The X100A base metal is the exception in which the flaw was positioned in the longitudinal direction and stress applied in the circumferential direction. K_{res} plotted for X100 welds, HAZ, and BM are identical to those in Fig. 7.

4. Conclusions

Five different high strength welds were fabricated from X100A base metal for the purpose of measuring fatigue crack growth rates (FCGR) in high pressure hydrogen gas. Test coupons were extracted from the weld regions along with select heat affected zones and FCGR were measured in 21 MPa H_2 at R_{app} =0.5 and frequency of 1 Hz. Identical test coupons were used to measure residual stresses by means of the slitting method. Residual stress, K_{res}, measurements were used to calculate the effect on stress ratio, $R_{tot}(a)$, and the FCGR curves were corrected to allow for residual stress-free FCGR curves. The residual stress-free curves displayed less variability than the raw data containing residual stress. Lower strength weld FCGR data from the literature were comparable to the high strength X100 welds which demonstrated, that despite differences in strength and microstructure, high strength welds are no more susceptible to hydrogen accelerated fatigue crack growth than the lower strength welds. An analysis was performed to compare the residual stress values measured via the slitting method on the test coupons versus recommended residual stress distributions from ASME FFS-1 [29] for low heat input welds. The results showed that the residual stresses measured in the test coupons were significantly lower than the recommend residual stress distributions for an intact welded pipe, highlighting that significant stress relaxation can occur through test coupon extraction. Quantifying and removing the residual stresses in FCGR data offers the greatest utility by providing a neutral starting ground for comparisons and design guidance when residual stress effects are to be considered.

5. Acknowledgments

The authors would like to thank the following people and funding agencies for their contributions to this work over the years. We would like to thank the technical support of the Hydrogen Effects on Materials Laboratory (HEML) at Sandia in Livermore, CA, specifically, Jeff Campbell, Brendan Davis, John Benton. We acknowledge the technical support from Doug Kyle, Brian T. Gibson, and Zhenggang Wu of ORNL for fabrication and characterization of the welds. Special thanks to Minh N. Tran (University of California, Davis) for computing residual stress intensity factors for the pipeline flaws. In addition, we would like to thank some collaborators from other institutions: Andy Slifka (NIST), Elizabeth Drexler (NIST, retired), Robert Amaro (Southern Company). This work was funded by the Fuel Cell Technology Office of DOE. Sandia National Laboratories is a multi-mission laboratory managed and operated by National Technology & Engineering Solutions of Sandia, LLC, a wholly owned subsidiary of Honeywell International Inc., for the U.S. Department of Energy's National Nuclear Security Administration under contract DE-NA0003525.

References:

[1] *Hydrogen Standardization Interim Report for Tanks, Piping, and Pipelines*, ASME, 2005.

[2] "U.S. DRIVE Hydrogen Delivery Technical Team Roadmap." https://www.energy.gov/sites/prod/files/2017/08/f36/hdtt_roadmap_July2017.pdf (accessed.

[3] J. A. Ronevich, C. R. D'Elia, and M. R. Hill, "Fatigue crack growth rates of X100 steel welds in high pressure hydrogen gas considering residual stress effects," *Engineering Fracture Mechanics,* vol. 194, pp. 42-51, 2018/05/01/ 2018, doi: https://doi.org/10.1016/j.engfracmech.2018.02.030.

[4] J. A. Ronevich, B. P. Somerday, and Z. Feng, "Hydrogen accelerated fatigue crack growth of friction stir welded X52 steel pipe," *International Journal of Hydrogen Energy,* vol. 42, no. 7, pp. 4259-4268, 2017/02/16/ 2017, doi: https://doi.org/10.1016/j.ijhydene.2016.10.153.

[5] J. A. Ronevich, B. P. Somerday, and C. San Marchi, "Effects of microstructure banding on hydrogen assisted fatigue crack growth in X65 pipeline steels," *International Journal of Fatigue,* vol. 82, no. Part 3, pp. 497-504, 2016/01/01/ 2016, doi: https://doi.org/10.1016/j.ijfatigue.2015.09.004.

[6] R. L. Amaro, N. Rustagi, K. O. Findley, E. S. Drexler, and A. J. Slifka, "Modeling the fatigue crack growth of X100 pipeline steel in gaseous hydrogen," *International Journal of Fatigue,* vol. 59, no. 0, pp. 262-271, 2014, doi: http://dx.doi.org/10.1016/j.ijfatigue.2013.08.010.

[7] A. J. Slifka *et al.*, "Fatigue crack growth of two pipeline steels in a pressurized hydrogen environment," *Corrosion Science,* vol. 78, no. 0, pp. 313-321, 2014, doi: http://dx.doi.org/10.1016/j.corsci.2013.10.014.

[8] R. L. Amaro, E. S. Drexler, and A. J. Slifka, "Fatigue crack growth modeling of pipeline steels in high pressure gaseous hydrogen," *International Journal of Fatigue,* vol. 62, no. 0, pp. 249-257, 2014, doi: http://dx.doi.org/10.1016/j.ijfatigue.2013.10.013.

[9] A. J. Slifka *et al.*, "Fatigue Measurement of Pipeline Steels for the Application of Transporting Gaseous Hydrogen," *Journal of Pressure Vessel Technology,* vol. 140, no. 1, pp. 011407-011407-12, 2017, doi: 10.1115/1.4038594.

[10] "Pipeline Accident Report NTSB/PAR-11/01 Pacific Gas and Electric Company Natural gas Transmission Pipeline Rupture and Fire, San Bruno, California," 2011.

[11] J. Ronevich and B. Somerday, "Hydrogen-Accelerated Fatigue Crack Growth in Arc Welded X100 Pipeline Steel," in *Materials Performance in Hydrogen Environments: Proceedings of the 2016 International Hydrogen Conference*, Jackson Hole, WY, B. P. Somerday and P. Sofronis, Eds., 2016: ASME, pp. 219-227.

[12] J. A. Ronevich and B. P. Somerday, "Assessing Gaseous Hydrogen Assisted Fatigue Crack Growth Susceptibility of Pipeline Steel Weld Fusion Zones and Heat Affected Zones," *Materials Performance and Characterization,* vol. 5, no. 3, pp. 290-304, 2016, doi: 10.1520/MPC20150057.

[13] A. Slifka *et al.*, "Measurements of Fatigue Crack Growth Rates of the Heat-Affected Zones of Welds of Pipeline Steels," presented at the Proceedings of ASME 2015 Pressure Vessels and Piping Conference, Boston, MA, 2015.

[14] Z. Feng, S. A. David, D. A. Tzelepis, and X. Yu, "Welding Method for Hydrogen Embrittlement Control," USA, 2016.

[15] B. P. Somerday, J. A. Campbell, K. L. Lee, J. A. Ronevich, and C. San Marchi, "Enhancing safety of hydrogen containment components through materials testing under in-service conditions," *International Journal of Hydrogen Energy,* vol. 42, pp. 7314-7321, 2017, doi: 10.1016/j.ijhydene.2016.04.189.

[16] *B31.12 Hydrogen Piping and Pipelines*, ASME, New York, NY, 2011.

[17] B. P. Somerday, P. Sofronis, K. A. Nibur, C. San Marchi, and R. Kirchheim, "Elucidating the variables affecting accelerated fatigue crack growth of steels in hydrogen gas with low oxygen concentrations," *Acta Materialia,* vol. 61, no. 16, pp. 6153-6170, 2013, doi: http://dx.doi.org/10.1016/j.actamat.2013.07.001.

[18] *E647-11 Standard Test Method for Measurement of Fatigue Crack Growth Rates*, ASTM, West Conshohocken, PA, 2011.

[19] M. B. Prime, "Residual stress measurement by successive extension of a slot: The crack compliance method," *Applied Mechanics Reviews,* vol. 52, no. 2, pp. 75-96, 1999.

[20] M. R. Hill, "The Slitting Method," in *Practical Residual Stress Measurement Methods*, G. S. Schajer Ed. West Sussex, UK: John Wiley & Sons, 2013, ch. 4, pp. 89-108.

[21] G. S. Schajer and M. B. Prime, "Use of Inverse Solutions for Residual Stress Measurements," *Journal of Engineering Materials and Technology,* vol. 128, no. 3, pp. 375-382, 2006, doi: 10.1115/1.2204952.

[22] H. J. Schindler, W. Cheng, and I. Finnie, "Experimental determination of stress intensity factors due to residual stresses," *Experimental Mechanics,* journal article vol. 37, no. 3, pp. 272-277, September 01 1997, doi: 10.1007/bf02317418.

[23] H. J. Schindler and P. Bertschinger, "Some steps towards automation of the crack compliance method to measure residual stress distributions," in *Fifth International Conference on Residual Stress*, 1997, pp. 682-687.

[24] J. K. Donald and D. A. Lados, "An integrated methodology for separating closure and residual stress effects from fatigue crack growth rate data," *Fatigue & Fracture of Engineering Materials & Structures,* vol. 30, no. 3, pp. 223-230, 2007, doi: doi:10.1111/j.1460-2695.2006.01081.x.

[25] M. James, K. Maciejewski, G. Wang, D. Ball, and R. Bucci, "A Methodology for Partitioning Residual Stress Effects From Fatigue Crack Growth Rate Test Data," 2016.

[26] J. K. Donald, G. H. Bray, and R. W. Bush, *Introducing the Kmax sensitivity concept for correlating fatigue crack growth data*. The Minerals, Metals and Materials Society, Warrendale, PA, 1997, pp. 123-141.

[27] S. Suresh and R. O. Ritchie, "Mechanisitic dissimilarities between environmentally influenced fatigue-crack propagation at near-threshold and higher growth rates in lower strength steels," *Metal Science,* vol. 16, pp. 529-538, 1982.

[28] *BS7910, Guide to methods for Assessing the Acceptability of Flaws in Metallic Structures*, B. S. Institution, 2015.

[29] *API 579-1/ASME FFS-1 2016 Fitness-For-Service*, ASME/API, 2016.

[30] *ASME BPVC Section XI Appendix A*, ASME, 2017.

[31] *ASME BPVC Section VIII Div 3 Article KD-4*, ASME, 2013.